Internally-Actuated Rovers for All-Access Surface Mobility: Theory and Experimentation

Ross Allen, Marco Pavone, Christopher McQuin, Issa A. D. Nesnas,
Julie C. Castillo-Rogez, Tam-Nguyen Nguyen, Jeffrey A. Hoffman

Abstract— The future exploration of small Solar System bodies will, in part, depend on the availability of mobility platforms capable of performing both large surface coverage and short traverses to specific locations. Weak gravitational fields, however, make the adoption of traditional mobility systems difficult. In this paper we present a planetary mobility platform (called "spacecraft/rover hybrid") that relies on internal actuation. A hybrid is a small ($\sim$ 5 kg), multi-faceted robot enclosing three mutually orthogonal flywheels and surrounded by external spikes or contact surfaces. By accelerating/decelerating the flywheels and by exploiting the low-gravity environment, such a platform can perform both long excursions (by hopping) and short, precise traverses (through controlled "tumbles"). This concept has the potential to lead to small, quasi-expendable, yet maneuverable rovers that are robust as they have no external moving parts. In the first part of the paper we characterize the dynamics of such platforms (including fundamental limitations of performance) and we discuss control and planning algorithms. In the second part, we discuss the development of a prototype and present experimental results both in simulations and on physical test stands emulating low-gravity environments. Collectively, our results lay the foundations for the design of internally-actuated rovers with controlled mobility (as opposed to random hopping motion).

I. INTRODUCTION

The recent Decadal survey report for planetary science has prioritized three main cross-cutting themes for planetary exploration: (1) the characterization of the early Solar System history, (2) the search for planetary habitats, and (3) an improved understanding about the nature of planetary processes [1]. A growing number of ground- and space-based observations indicate that the exploration of a selected subset of *small* Solar System bodies would collectively address all such themes [2]. The exploration of small bodies, such as Near Earth Objects and Martian moons, is also a key

Ross Allen and Marco Pavone are with the Department of Aeronautics and Astronautics, Stanford University, Stanford, CA 94305 {`rallen10`, `pavone`}`@stanford.edu`.

Julie C. Castillo-Rogez, Christopher McQuin, and Issa A. D. Nesnas are with the Jet Propulsion Laboratory, California Institute of Technology, Pasadena, CA 91109 {`julie.c.castillo`, `christopher.mcquin`, `issa.a.nesnas`}`@jpl.nasa.gov`.

Jeffrey A. Hoffman and Tam-Nguyen Nguyen are with the Department of Aeronautics and Astronautics, Massachusetts Institute of Technology, Cambridge, MA 02139, {`jhoffma1`, `tamz`}`@mit.edu`.

component of the flexible path for Human exploration. In general, science of the early Solar System and the search for habitats revolve around characterizing planetary material chemistry (elemental, isotopic, mineralogical, noble gas, organics, etc.). While some measurements can be obtained with remote platforms (such as space telescopes or orbiters), several other measurements require direct contact with (or close proximity to) the surface for an *extended* period of time at *multiple* locations [2]. This is also the case for precursor science enabling Human exploration, which requires the characterization of regolith mechanical properties, dust dynamics and electrostatic charging [3]. Hence, in-situ exploration of small bodies at multiple designated locations is an important need in the scientific community and is best achieved with surface mobility.

On the other hand, weak gravitational fields (micro-g to milli-g), which are characteristic of small bodies, make the adoption of traditional mobility systems difficult. Specifically, mobility mechanisms for micro-gravity environments can be broadly divided into four classes, namely, mobility via thrusters, wheeled mobility, legged mobility, and hopping mobility. Mobility via thrusters (see, e.g., [4]) is characterized by mechanical and operational complexity (e.g., hovering at very low gravities is challenging), might lead to surface contamination (due to firing thrusters), and is likely to involve risk due to surface ejecta. On the other hand, in low-gravity environments wheeled vehicles are bound to extremely low speeds (less than 1.5mm/s [5]) due to low traction and surface bumps which can cause loss of surface contact and uncontrolled tumbling. Alternatively, legged systems are mechanically complex and highly dependent on soil properties [6], [7], which are largely unknown. Finally, there are two basic principles of hopping: (#1) the hopper uses a sticking mechanism (thus jumping away from the surface), and (#2) the hopper moves an internal mass. NASA, RKA, ESA, and JAXA have all recognized the advantages of hopping on small bodies. However, both of NASA's hopper prototypes [5], [8] (that rely on a combination of wheels and sticking mechanisms), ESA's hopper prototype (that hops by spinning two eccentric masses [9]), RKA's lander for the failed exploration of Phobos (that hops by sticking the surface [10], but was not deployed due to failure of *Phobos* 2), and JAXA's MINERVA lander (that hops by rotating a single flywheel mounted on a turntable and did not succeed during its deployment [11]) do not allow for precise traverses to designated targets in low gravity environments. Key advantages of hopping platforms include

relatively simple actuation, ability to cover a large surface, and relative insensitivity to soil characteristics. Furthermore, internal actuation (when hopping according to principle (#2)) reduces the problem of dust contamination in the actuators and simplifies thermal control. For these reasons, it has been argued that, *if one is able to include the option of fine mobility*, hopping robots with internal actuation could represent a good trade-off between performance and complexity [12] (despite issues related to instrument pointing).

Accordingly, in this paper, we study microgravity rovers that rely on *internal actuation* (i.e., which propel themselves by moving/spinning internal masses), and are capable of performing both large surface coverage *and* short traverses to specific locations. Specifically, the contribution of this paper is fourfold. First, we describe a mobility platform, called "spacecraft/rover hybrid", which generates motion via actuation of three, internal, mutually orthogonal flywheels (Section II). By accelerating/decelerating the flywheels and by exploiting the low-gravity environment, a hybrid can perform both long excursions (by hopping) *and* short traverses to specific locations (through a sequence of controlled "tumbles"). Second, we characterize the dynamics of such platforms, including fundamental limitations of performance, e.g., in terms of forward speed (Section III), and we discuss planning and control algorithms (Section IV). Third, we discuss the development of a prototype and design considerations (Section V). Finally, we present experimental results both in numerical simulations and on physical test stands emulating low-gravity environments (VI). Collectively, our results lay the foundations for the design of internally-actuated rovers with controlled mobility (as opposed to random hopping motion) in low-gravity environments.

II. MOBILITY PLATFORM

A spacecraft/rover hybrid is a small (≈ 0.4 m geometrical diameter, ≈ 5kg even though the design is scalable) multi-faceted geometric solid that encloses three mutually orthogonal flywheels and is surrounded by external spikes or specialized contact surfaces (see Figure 1, where we consider a cube geometry; design considerations are discussed in detail in Section V). Specifically, there is no external propulsion. The combination of the flywheels with the enclosure- and spike-geometry enables controlled tumbles, hops, and high-altitude ballistic flight.

The basic principle behind a flywheel is the conservation of angular momentum, which ensures that angular momentum can be swapped between the platform and the flywheels. Specifically, a flywheel consists of a spinning mass with a substantial amount of inertia. Due to the presence of the flywheels, the total angular momentum of the platform is given by (vectors and matrices are represented in boldface):

$$\mathbf{H} = \mathbf{I}_{\text{platform}}\, \boldsymbol{\omega}_{\text{platform}} + \sum_{i=1}^{3} \mathbf{I}_{\text{flywheel},i}\, \boldsymbol{\omega}_{\text{flywheel},i},$$

where $\mathbf{I}$ denotes the inertia matrix and $\boldsymbol{\omega}$ denotes the angular velocity vector. Since, in absence of *external* torques, the total angular momentum stays constant, by controlling the

internal torque between the flywheels and the platform one can control both magnitude and direction of the angular rotation of the platform. In turn, this angular rotation can give rise to (controllable) surface reaction forces at contact points, which lead to either tumbling (i.e., pivoting around a tip) or hopping (when the reaction forces are large enough). The next section presents a 2D analytical model (amenable to analytical treatment) where collisions with ground are assumed inelastic and impulsive, and a 3D model (studied numerically) where contact interactions are modeled according to a spring-damper combination.
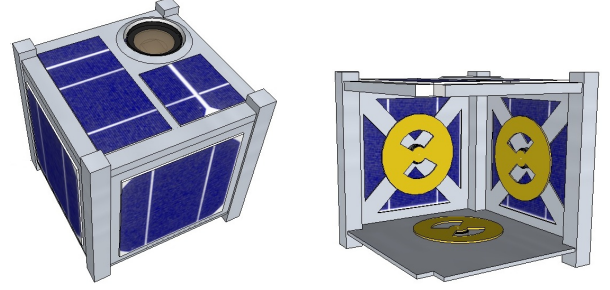

Fig. 1. A spacecraft/rover hybrid is a planetary mobility platform sealed in one enclosure and actuated through three mutually orthogonal flywheels (for clarity, internal payload is not shown). By spinning the flywheels, one gives rise to surface reaction forces that make the rover tumble or hop. External spikes/feet (not shown here for clarity) are added to protect instruments and solar panels, and to improve traction. Trade-offs for spike design are discussed in Section V.
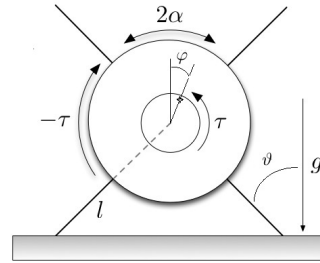
	Definition
ϑ	hybrid's angle
φ	flywheel's angle
m_{rw}	mass of platform
m_{fw}	mass of flywheel
l	spikes' length
r_{rw}	radius of platform
r_{fw}	radius of flywheel
τ	flywheel's torque
2α	angle in between spikes
g	gravity acceleration

Fig. 2. Analytical model; collisions with ground are inelastic and impulsive.

III. DYNAMICS OF A HYBRID

In this section we present both a 2D and a 3D model for a hybrid.

A. 2D Analytical Model

In the analytical model, the hybrid is modeled in 2D as a disk with equispaced rigid spikes attached to it; a motor, attached at its center of mass, drives a single disk-shaped flywheel (see Figure 2). We use a disk shape since this leads to slightly simpler formulas; the results we obtain, however, represent a reasonable approximation for other symmetrical geometries (e.g., squares) with the same geometrical diameter. The key assumptions in this model are: (1) collisions with ground are inelastic and impulsive (only angular momentum is conserved around the point of collision, and the spike sticks to the ground); (2) the stance foot acts as a pin joint

and does not slip, and (3) the transfer of support at the time of contact is instantaneous (no double support phase). This model is inspired by work in the field of passive dynamic walking [13], [14] and, specifically, is based on the model in [15]. With this model we aim to characterize the 2D tumbling motion, in particular, required torques, momentum unloading strategies, and bounds on achievable speeds in microgravity. Even though the assumptions of this model are somewhat unrealistic (especially on small bodies), the results we obtain provide valuable first-order estimates for the aforementioned quantities (as also confirmed by experiments reported in Section VI).

1) Tumbling motion: The 2D flywheel-driven hybrid has two states, namely the angle ϑ between the stance spike and the vertical and the angle φ of a reference point on the flywheel with respect to the vertical (see Figure 2); note that we use the convention that angles increase in the clockwise direction. The parameters of the system are defined in Figure 2.

The goal of the control strategy for the flywheel is to cause the platform to tumble to the right, stepping from spike to spike. A complete step is composed of a *stride* phase and a *collision* phase [15]. The stride phase occurs when the system is supported by a single spike. The collision phase occurs when the next consecutive spike collides with the ground. We first consider the stride phase. The equations of motion are those of an inverted pendulum and can be written as

$$\ddot{\vartheta}(t) = \frac{(m_{\mathrm{rw}} + m_{\mathrm{fw}})g\,l\sin(\vartheta(t)) - I_{\mathrm{fw}}\ddot{\varphi}(t)}{(m_{\mathrm{rw}} + m_{\mathrm{fw}})l^2 + I_{\mathrm{rw}}}. \quad (1)$$

In our model we assume that the motor is a conventional DC motor and that, as is typical, there is a fast inner feedback loop to control the current. Hence, the armature current is our control input. Since the armature current is linked to the flywheel's acceleration (assuming negligible friction) through a scale factor, henceforth we will consider as *equivalent* input the flywheel's acceleration.

Second, we consider the equations of motion during the collision phase. The angular momentum (about the contact point) of the system evolves according to the equation: $\mathbf{L}(t) = \mathbf{L}(t_0) + \int_{t_0}^{t} \mathbf{T}_{\mathrm{ext}}(t)\,dt$, where $\mathbf{T}_{\mathrm{ext}}(t)$ represents the external torques acting on the system. During impact the only external torque is due to gravity (all other torques are internal and cancel each other), and is given by $\mathbf{T}_{\mathrm{ext}}(t) = (m_{\mathrm{rw}} + m_{\mathrm{fw}})g\,l\sin(\vartheta(t))(-\mathbf{e}_z)$ (where $\mathbf{e}_z$ is the unit normal vector outward from the plane). Since $\|\mathbf{T}_{\mathrm{ext}}(t)\| \leq (m_{\mathrm{rw}} + m_{\mathrm{fw}})g\,l\sin(\alpha)$ and since the collision with the ground is impulsive (i.e., the collision time dt approaches zero), during a collision the angular momentum is (approximately) conserved. The conservation of angular momentum during collision allows for the determination of the initial state for the next stride phase. Specifically, the angular momentum about the collision point of next spike immediately before collision is $\mathbf{L}(t^-) = (m_{\mathrm{rw}} + m_{\mathrm{fw}})\dot{\vartheta}(t^-)l^2\cos(2\alpha)(-\mathbf{e}_z) + I_{\mathrm{rw}}\dot{\vartheta}(t^-)(-\mathbf{e}_z) + I_{\mathrm{fw}}\dot{\varphi}(t^-)(-\mathbf{e}_z)$, while the angular momen-

tum about the collision point of next spike immediately after collision is $\mathbf{L}(t^+) = (m_{\mathrm{rw}} + m_{\mathrm{fw}})\dot{\vartheta}(t^+)l^2(-\mathbf{e}_z) + I_{\mathrm{rw}}\dot{\vartheta}(t^+)(-\mathbf{e}_z) + I_{\mathrm{fw}}\dot{\varphi}(t^+)(-\mathbf{e}_z)$. Assuming that $\ddot{\varphi}(t)$ is a bounded function (as it is true for any physical system), one has $\dot{\varphi}(t^-) = \dot{\varphi}(t^+)$, and therefore equating the magnitudes of $\mathbf{L}(t^-)$ and $\mathbf{L}(t^+)$ one obtains:

$$\dot{\vartheta}(t^+) = \frac{(m_{\mathrm{rw}} + m_{\mathrm{fw}})l\,\cos(2\alpha) + I_{\mathrm{rw}}}{(m_{\mathrm{rw}} + m_{\mathrm{fw}})l + I_{\mathrm{rw}}}\,\dot{\vartheta}(t^-). \quad (2)$$

Hence, the angular velocity for the next stride phase is reduced (by a factor $\cos(2\alpha)$ if I_{rw} is negligible), as it is expected since collisions are assumed inelastic. As in [13], [15], we define η as the loss coefficient for the angular speed, i.e.,

$$\eta := \frac{\dot{\vartheta}(t^+)}{\dot{\vartheta}(t^-)} = \frac{(m_{\mathrm{rw}} + m_{\mathrm{fw}})l\,\cos(2\alpha) + I_{\mathrm{rw}}}{(m_{\mathrm{rw}} + m_{\mathrm{fw}})l + I_{\mathrm{rw}}}.$$

We consider next three cases of increasing complexity, namely: unactuated flywheel, constant actuation, and time-varying actuation. When the flywheel is unactuated (i.e., $\ddot{\varphi}(t)$ is identically zero during the stride), the minimum initial angular speed to vault the hybrid over the stance spike and take a step is:

$$\omega_{\mathrm{min}} := \sqrt{\frac{2(m_{\mathrm{rw}} + m_{\mathrm{fw}})g\,l(1 - \cos(\alpha))}{(m_{\mathrm{rw}} + m_{\mathrm{fw}})l^2 + I_{\mathrm{rw}}}}.$$

According to the loss equation (2), an unactuated hybrid will asymptotically come to rest. The aim of the flywheel controller is then to regain, during the stride phase, the speed lost during the impact.

The simplest possible actuation for the flywheel is to have a constant acceleration during the stride phase (i.e., $\ddot{\varphi}(t) = \ddot{\overline{\varphi}} < 0$, negative because it is opposite to tumbling direction). Assume that the angular speed at the beginning of a stride phase is $\dot{\vartheta}(0) := \omega_{\mathrm{ini}} \geq \omega_{\mathrm{min}}$; by using energy arguments, one can easily show that the required acceleration to maintain the same angular speed at the beginning of each subsequent stride phase is:

$$\ddot{\overline{\varphi}} = -\dot{\vartheta}^2(0)\frac{\frac{1}{2}\big[(m_{\mathrm{rw}} + m_{\mathrm{fw}})l^2 + I_{\mathrm{rw}}\big](1/\eta^2 - 1)}{2\alpha I_{\mathrm{fw}}}, \quad (3)$$

which depends on gravity since we assumed $\dot{\vartheta}(0) \geq \omega_{\mathrm{min}}$. Figure 3(a) shows the magnitude of the minimum torques for a Phobos-like environment (i.e. g in the 0.001 m/s^2 range). Assuming that the flywheel is powered by a "conventional" DC motor, one can conclude that for a gravity level similar to the one on Phobos the power consumption is about $2 - 5$ Watts. The corresponding linear velocity for tumbling is about 0.05 m/s (Phobos's escape velocity is about 11 m/s). Clearly, this control strategy is not physically realizable since the flywheel will eventually reach a *saturation* speed. It is of interest to characterize the number of strides the flywheel can operate before it saturates. To first order terms, the duration of a stride is given by $\tau_{\mathrm{stride}} = 2\alpha/\dot{\vartheta}(0)$. Hence, if $\dot{\varphi}_{\mathrm{max}}$ is the maximum angular speed of the flywheel, the system can

(a) Torques for *tumbling* motion. Left figure: torque vs. spikes' length (gravity $g = 0.001$ m/s^2). Right figure: torque vs. gravity (spikes' length $l = 0.4$ m).

(b) Torques for *hopping* motion. Left figure: torque vs. spikes' length (gravity $g = 0.001$ m/s^2). Right figure: torque vs. gravity (spikes' length $l = 0.4$ m).
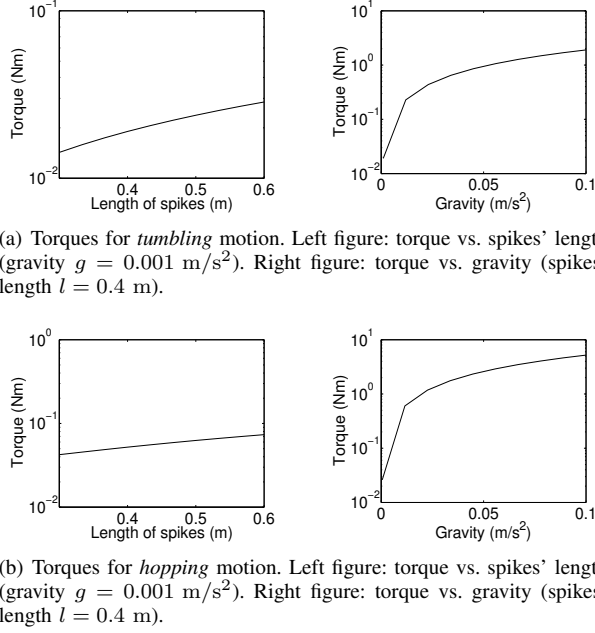
Fig. 3. Minimum torques for tumbling and hopping motion (the y-axis is in logarithmic scale). System's parameters: platform's mass equal to 2.9 kg, flywheel's mass equal to 0.1 kg (hence the total mass is 3 kg), radius of platform equal to 0.2 m, and 4 spikes (hence $\alpha = \pi/4$). Longer spikes facilitate tumbling over large rocks but require higher torques.

operate for a number of cycles (i.e., strides) equal to:

$$N_{\max} = \frac{2\,\dot{\varphi}_{\max}\,I_{\text{fw}}}{\dot{\vartheta}(0)[(m_{\text{rw}}+m_{\text{fw}})l^2 + I_{\text{rw}}](1/\eta^2 - 1)}.$$

For a Phobos-like environment (i.e. g in the 0.001 m/s^2 range), assuming that the maximum rpm for the flywheel motor is 10,000, the maximum number of cycles is then equal to $\simeq 160$ (or about 150 m). A few comments are in order. First, one can see that with realistic values for the system parameters (e.g., the gravity acceleration is similar to that of Phobos) the platform can tumble at an average speed of 3 cm/s for about 150 m drawing a current of about 0.002 A. Second, the formula for the constant acceleration control (equation (3)) shows that such value depends quadratically on the length of the spikes, hence there is an important tradeoff between the capability of negotiating obstacles (that would require long spikes) and the amount of actuation (that prefers short spikes). Third, the actuation level depends quadratically on the desired angular speed. Fourth, as already mentioned, the above control strategy has the disadvantage that after some time the flywheel will reach the saturation limit for its speed. This issue will be addressed in more detail at then end of this section.

Finally, by allowing a time-varying actuation for the flywheel, one can guarantee, perhaps surprisingly, that the angular speed of both the platform *and* the flywheel are the same at the beginning of each stride (i.e., there is forward motion but no net increase in flywheel's speed). Following [15], this can be achieved through a 4-step control strategy: 1) while ϑ is negative the flywheel is negatively accelerated

($\ddot{\varphi} < 0$); 2) when ϑ becomes positive the flywheel is positively accelerated (i.e., $\ddot{\varphi} > 0$) in such a way that the rotation of the system is stopped (i.e., $\dot{\vartheta} = 0$) and for a certain interval of time (depending on η) angular momentum is accumulated; 3) the flywheel is negatively accelerated to quickly reduce its speed to the initial speed; 4) the flywheel is then left unactuated until collision (i.e., until $\vartheta = \alpha$).

It is of interest to characterize the fundamental limitations of performance for control policies that avoid a build-up in flywheel's velocity. By rather simple angular momentum arguments (see [15, page 24] for the details of a very similar derivation), one can show that a hybrid undergoing a steady-state (i.e., with equal angular velocity at each start of stride) tumbling motion with zero initial and final flywheel speeds and with non-negative net flywheel rotation can travel at a ground speed no larger than:

$$v_{\max} := \frac{2l\sin(\alpha)\,(m_{\text{rw}}+m_{\text{fw}})\,g\,l\,\sin(\alpha)}{\sqrt{2\alpha\,(1-\eta)[(m_{\text{rw}}+m_{\text{fw}})l^2 + I_{\text{rw}}]}}.$$

For a Phobos-like environment and hybrid's parameters as in Figure 3, $v_{\max} \approx 5$ cm/s.

2) Hopping: A very similar analysis can be performed for the hopping motion. Specifically, we study the following model: a hybrid starts by rotating around a spike according to the tumbling motion described in the previous section. When the next spike impacts the ground, we still assume that the collision is impulsive and inelastic and that the transfer of support is instantaneous; however, we do not constrain the new stance foot to act as a pin joint, and we study the minimum angular speed that makes the hybrid "hop" or, more precisely, makes the stance foot complete a rotation of 2α without contacting the ground. One can show that hopping is achieved with a constant flywheel deceleration (assuming no saturation) equal to:

$$\ddot{\varphi} \leq -\frac{g}{I_{\text{fw}}}\min\left\{(m_{\text{rw}}+m_{\text{fw}})l\,\sin(\alpha),\, \frac{(m_{\text{rw}}+m_{\text{fw}})l^2 + I_{\text{rw}}}{4\,\eta^2\,l\,\cos(\alpha)\,\alpha}\right\}.$$

Figure 3(b) shows the magnitude of the minimum torques for a Phobos-like environment.

3) Desaturation strategies for the flywheel: A key feasibility aspect for such mobility concept is flywheel's speed saturation. The simple 2D model suggests several strategies to mitigate this problem. The first and second strategies were previously discussed: operate without consideration of saturation; and careful acceleration and deceleration of the flywheel such that forward motion is produced without a net increase in flywheel speed. The first strategy is reasonable for very low gravity and/or moderate coverage requirements (≈ 100 m for Phobos-like conditions). The second is most effective, but requires sophisticated sensing and control. Third strategy: after a certain number of tumbles/hops, the flywheel is slowly despun in such a way that the platform does not tip over. This strategy is simple but substantially decreases the hybrid's average speed. Fourth strategy (in some sense dual of the third strategy): the flywheel is slowly accelerated (such that the platform does not tip over) and then decelerated in a very short time interval (by using brakes).

In this way the hybrid starts a hop/tumble with a flywheel angular velocity of zero. This strategy is further developed in Section IV.

B. 3D Numerical model

Prior work on microgravity mobility has either simulated dynamics of rigid bodies without motion planning [9], [16], or studied planning algorithms for mobility platforms modeled as point masses [17]. In this section we present a 3D model for the hybrids that will be used in Section IV to develop planning algorithms on a realistic, rigid body representation of the hybrid. This model allows for the elimination of some of the assumptions required for the analytical model (e.g., single contact point acting as a pivot). By extending the work in [18], the Newtonian equations for the equations of motion for the hybrid (including the internal flywheels) are as follows (the notation is defined in Table I):

- Position and velocity:

$$
{}^{b}\dot{\mathbf{r}}_{cm} = {}^{b}\mathbf{v}_{cm},
$$
$$
{}^{b}\dot{\mathbf{v}}_{cm} = \frac{\mathbf{F}}{m_{tot}} - 2\left({}^{I}\mathbf{\Omega}_{bd} \times {}^{b}\mathbf{v}_{cm}\right) - \left({}^{I}\alpha_{bd} \times {}^{b}\mathbf{r}_{cm}\right) -
$$
$$
{}^{I}\mathbf{\Omega}_{bd} \times \left({}^{I}\mathbf{\Omega}_{bd} \times {}^{b}\mathbf{v}_{cm}\right).
$$

- Euler parameters:

$$
\begin{bmatrix} {}^{b}\dot{\epsilon}_1 \\ {}^{b}\dot{\epsilon}_2 \\ {}^{b}\dot{\epsilon}_3 \\ {}^{b}\dot{\epsilon}_4 \end{bmatrix} = \frac{1}{2} \begin{bmatrix} {}^{b}\epsilon_4 & -{}^{b}\epsilon_3 & {}^{b}\epsilon_2 & {}^{b}\epsilon_1 \\ {}^{b}\epsilon_3 & {}^{b}\epsilon_4 & -{}^{b}\epsilon_1 & {}^{b}\epsilon_2 \\ -{}^{b}\epsilon_2 & {}^{b}\epsilon_1 & {}^{b}\epsilon_4 & {}^{b}\epsilon_3 \\ -{}^{b}\epsilon_1 & -{}^{b}\epsilon_2 & -{}^{b}\epsilon_3 & {}^{b}\epsilon_4 \end{bmatrix} \begin{bmatrix} {}^{b}\omega_1 \\ {}^{b}\omega_2 \\ {}^{b}\omega_3 \\ 0 \end{bmatrix}.
$$

- Angular velocities:

$$
\begin{bmatrix} I_1 & 0 & 0 & J_B\beta_{B_1} & J_C\beta_{C_1} & J_D\beta_{D_1} \\ 0 & I_2 & 0 & J_B\beta_{B_2} & J_C\beta_{C_2} & J_D\beta_{D_2} \\ 0 & 0 & I_3 & J_B\beta_{B_3} & J_C\beta_{C_3} & J_D\beta_{D_3} \\ \beta_{B_1} & \beta_{B_2} & \beta_{B_3} & 1 & 0 & 0 \\ \beta_{C_1} & \beta_{C_2} & \beta_{C_3} & 0 & 1 & 0 \\ \beta_{D_1} & \beta_{D_2} & \beta_{D_3} & 0 & 0 & 1 \end{bmatrix} \begin{bmatrix} {}^{I}\dot{\omega}_1 \\ {}^{I}\dot{\omega}_2 \\ {}^{I}\dot{\omega}_3 \\ {}^{s}\dot{\omega}_B \\ {}^{s}\dot{\omega}_C \\ {}^{s}\dot{\omega}_D \end{bmatrix} =
$$
$$
\begin{bmatrix} M_1 + (I_2 - I_3)\,{}^{I}\dot{\omega}_2\,{}^{I}\dot{\omega}_3 + \sum\limits_{k=B,C,D}\left(J_k\,{}^{s}\omega_k\left(\beta_{k_2}\,{}^{I}\omega_3 - \beta_{k_3}\,{}^{I}\omega_2\right)\right) \\ M_2 + (I_3 - I_1)\,{}^{I}\dot{\omega}_3\,{}^{I}\dot{\omega}_1 + \sum\limits_{k=B,C,D}\left(J_k\,{}^{s}\omega_k\left(\beta_{k_3}\,{}^{I}\omega_1 - \beta_{k_1}\,{}^{I}\omega_3\right)\right) \\ M_3 + (I_1 - I_2)\,{}^{I}\dot{\omega}_1\,{}^{I}\dot{\omega}_2 + \sum\limits_{k=B,C,D}\left(J_k\,{}^{s}\omega_k\left(\beta_{k_1}\,{}^{I}\omega_2 - \beta_{k_2}\,{}^{I}\omega_1\right)\right) \\ \dfrac{{}^{s}\mathbf{M}_B \cdot \vec{\beta}_B}{J_B} \\ \dfrac{{}^{s}\mathbf{M}_C \cdot \vec{\beta}_C}{J_C} \\ \dfrac{{}^{s}\mathbf{M}_D \cdot \vec{\beta}_D}{J_D} \end{bmatrix}.
$$

The external loads, $\mathbf{F}$, and external moments, $\mathbf{M}$, are calculated according to a simple spring-damper-friction contact model. The force normal to the ground is modeled as a spring-damper system and transverse forces are calculated using a Coulomb friction model. While these models are reasonably accurate for hard surfaces, soft, granular media (as it is the case for regoliths) requires a more sophisticated contact model, which is left for future work.

In the above dynamics equations, except for the terms ${}^{s}\mathbf{M}_k \cdot \vec{\beta}_k$, all of the variables are either state variables, or contact forces that are found by solving the set of differential equations, or terms that are known a priori. Each ${}^{s}\mathbf{M}_k \cdot \vec{\beta}_k$ term represents the torque applied along the central axis of

	Definition
${}^{b}\mathbf{r}_{cm}$	position of spacecraft cm w.r.t. celestial body
${}^{b}\mathbf{v}_{cm}$	velocity of spacecraft cm w.r.t. celestial body
$\mathbf{F}$	net external force on spacecraft
m_{tot}	total mass of spacecraft w/ flywheels
${}^{I}\mathbf{\Omega}_{bd}$	angular velocity of celestial body w.r.t. inertial
${}^{I}\alpha_{bd}$	angular acceleration of celestial body w.r.t. inertial
${}^{b}\epsilon_i$	i^{th} Euler orientation parameter w.r.t. celestial body
${}^{b}\omega_i$	i^{th} angular velocity of craft w.r.t. celestial body
${}^{I}\omega_i$	i^{th} angular velocity of craft w.r.t. inertial
I_i	i^{th} principle MOI of craft about cm
J_k	axial MOI of flywheel k (k = B, C, D)
$\vec{\beta}_k$	axis of rotation of flywheel k w.r.t. spacecraft
${}^{s}\omega_k$	angular velocity of flywheel k w.r.t. spacecraft
${}^{s}\mathbf{M}_k$	torque on flywheel k from spacecraft
M_k	i^{th} component of net external torque on spacecraft

TABLE I

NOTATION FOR THE DYNAMICS EQUATIONS.

the kth flywheel and acts as one of the control inputs to the system. A predetermined profile of the control variables must be fed into the system (open-loop control), or closed-loop control must be used to generate these values during the simulation. Section IV details a closed-loop, hybrid approach for the flywheels to achieve waypoint tracking.

IV. PLANNING AND CONTROL

The current computational model is restricted to uniform gravity fields and perfectly spherical terrain. Even under these idealized conditions, motion planning and control is still a significant challenge. The main difficulties stem from the gyroscopic coupling of the rotational degrees of freedom due to flywheel motion, and the unpredictable nature of hopping/bouncing due to the hybrid's non-spherical shape.

Our approach consists of a simple 3-mode hybrid control algorithm, whereby the flywheels are slowly accelerated to a desired angular velocity (referred to as "objective net angular velocity"), and then impulsively braked to generate the torque needed to produce hopping/tumbling. Figure 4 diagrams the control modes and the switching conditions.

Specifically, the key idea behind the proposed motion planning algorithm is that the net angular velocities of the flywheels prior to braking should form a vector that is mutually orthogonal to both the heading and local gravity vectors. In this way, the torque from braking the flywheels causes the hybrid to tumble or hop in the general direction of the next waypoint. Deviations from the intended hopping direction, caused by a non-spherical geometry (e.g. edges, spikes), are compensated for by applying this approach to a sequence of hops/tumbles. Accordingly, the direction of the objective net flywheel angular velocity prior to braking is

$$
\hat{\omega}_{objective} = \frac{\vec{h} \times \vec{g}}{\left|\vec{h} \times \vec{g}\right|}, \tag{4}
$$

where $\hat{\omega}_{objective}$ is the unit vector of the objective net angular velocity of flywheels, $\vec{g}$ is the local gravity vector, and $\vec{h}$ is the heading vector to the next waypoint (see Figure 5).
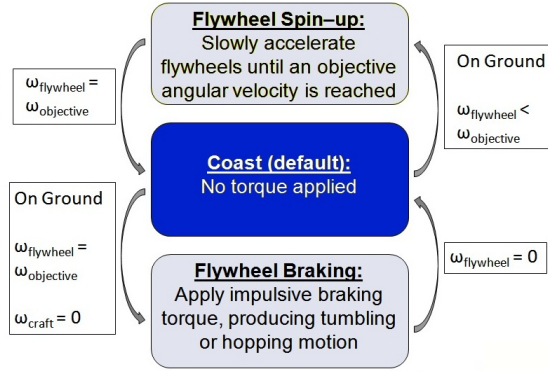
Fig. 4. Hybrid control algorithm: controlled mobility is achieved by slowly accelerating and then impulsively braking the flywheels. The angular velocity to which each flywheel is accelerated is determined by the hybrid orientation and intended heading. Additional control is used to ensure unwanted tumbling does not occur during the Spin-up mode.

Fig. 5. The net angular velocities of the flywheels prior to braking ($\hat{\omega}_{\text{objective}}$) should form a vector that is roughly anti-parallel to the net torque on the flywheels during braking (yellow arrow in above figure). This set of vectors is defined to be mutually orthogonal to both the heading and local gravity vectors according to equation (4).

The *magnitude* Ω of the objective net angular velocity of the flywheels is calculated according to two rather natural guidelines: (1) the hybrid attempts to travel from its current location to the next waypoint via an ideal hop (45° launch vector), and (2) the rotational kinetic energy stored in the flywheels before braking is approximated as equal to the translational kinetic energy of the hybrid after braking. A brief comment on these guidelines: they are fundamentally approximations (i.e. the hybrid does *not* travel to each waypoint via a single hop and the two energy terms are not exactly equal), however their enforcement leads to a simple, yet effective computation of the control inputs. Specifically, let v_0 be the velocity of the hybrid just after braking; according to guideline (1), $v_0^2 = gh$, where h is the distance to be traveled. Applying guideline (2), we obtain:

$$\underbrace{\frac{1}{2} k_p m_{tot} v_0^2}_{\text{translational}} = \underbrace{\sum \frac{1}{2} I_k \omega_k^2}_{\text{rotational}},$$

where ω_k is the angular velocity of the kth flywheel prior to braking, m_{tot} is the total mass of the hybrid ($m_{\text{rw}} + \sum m_{\text{fw},k}$), and the control gain k_p is used to account for energy losses. Since, by definition, $\omega_k = \Omega \, \hat{\omega}_{\text{objective}} \cdot \vec{\zeta}_k$, where $\vec{\zeta}_k$ is the unit vector of the kth flywheel's central axis, one can readily solve for Ω as

$$\Omega = \sqrt{\frac{k_p m_{tot} \, gh}{\sum I_k \left(\hat{\omega}_{\text{objective}} \cdot \vec{\zeta}_k \right)^2}}.$$

The objective angular velocity for each flywheel is then:

$$\omega_k = \left(\sqrt{\frac{k_p m_{tot} \, gh}{\sum I_k \left(\hat{\omega}_{\text{objective}} \cdot \vec{\zeta}_k \right)^2}} \right) \hat{\omega}_{\text{objective}} \cdot \vec{\zeta}_k. \quad (5)$$

Once the objective angular velocities are determined (by using equations (4) and (5)), the flywheels are slowly accelerated to these velocities so as to ensure that unwanted tumbling (i.e. tumbling away from the next waypoint) does
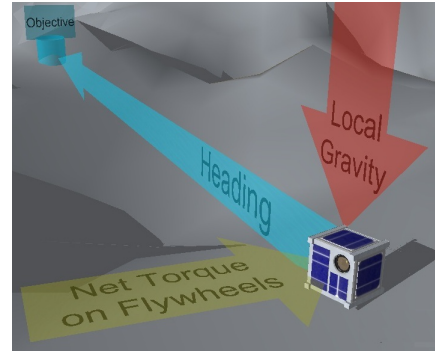
not occur. The analytical model of the hybrid (see Section III) is used to estimate the maximum torque that does not induce tumbling. Feedback control is then used to ensure that tumbling does not occur during the flywheel spin-up. Once the objective angular velocities are reached, brakes are applied to the flywheels to induce hopping motion. An upper bound is put on the flywheel velocities to model flywheel saturation and a lower bound is imposed on the objective angular velocity to ensure that some motion occurs for each spin-and-brake sequence. No control is applied while the hybrid is in ballistic flight or while it is coming to a rest. This process is repeated until the hybrid comes to rest within a tolerance region of each waypoint. Successful execution of this algorithm for four arbitrary waypoints is displayed and discussed in Figure 6. Our simulation results assume a smooth surface; future work will address the case of rocky terrains and non-uniform gravity levels.

V. PROTOTYPE AND DESIGN CONSIDERATIONS

A first generation of spacecraft/rover hybrids was developed to validate the results of the computer simulations. The prototype and CAD models for the structure and the flywheels are given in Figure 7. The design includes one internal motor/flywheel combination aligned with the unconstrained rotational degree of freedom on the passive gravity off-load test stand (that consists of a gravity off-load system of pulleys and a counterweight; more details about the test stand are provided in Section VI). The test vehicle also includes an Arduino microcontroller to coordinate motion and capture data, an 11.9V DC battery for power, and an electronic speed controller. An optical rpm sensor measures and records flywheel speeds, and the torques applied during experimentation are calculated as $\tau_{\text{applied}} = I_{\text{fw}} \alpha_{\text{fw}}$.

The motor/flywheel subsystem consists of a brushless DC motor capable of spinning the flywheel at up to 12,000 rpm. All components in the system were designed with that maximum speed in mind. The flywheel was designed to be as close as possible to the center of the vehicle without interfering with the proposed additional flywheels in the full 3-axis vehicle. The result is a tapered flywheel that balances

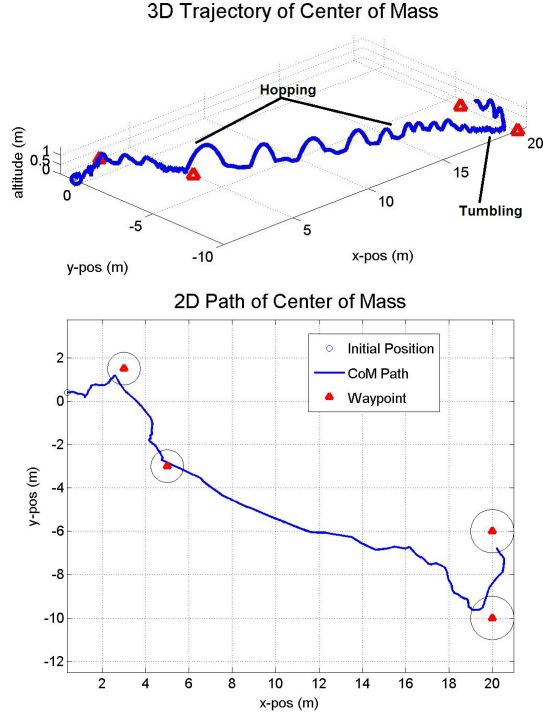3D Trajectory of Center of Mass

2D Path of Center of Mass

Fig. 6. Demonstration of *controlled* mobility (as opposed to random hopping motion): the plots represent the application of the motion planning and control algorithm under Phobos-like conditions (i.e., gravity levels in the order of $\mathrm{mm/s^2}$). Waypoints were selected to demonstrate short and long traverses and directional changes. The hybrid averages a velocity of $\approx 1.6\mathrm{cm/s}$ over the 1770 seconds it takes to visit the four waypoints. This velocity compares well with the analytical result from Section III which established a maximum achievable tumbling velocity of $\approx 5\mathrm{cm/s}$.
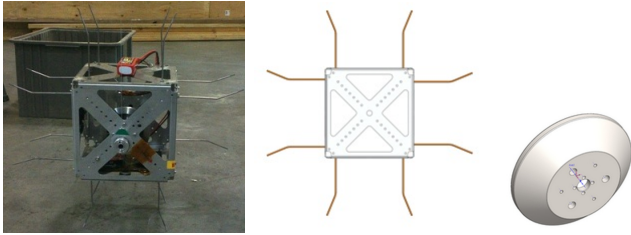

Fig. 7. Prototype and CAD models (not to scale). The prototype, without the flywheel, has a mass of 1.39 kg and a moment of inertia about the axis of rotation of ≈ 0.054 $\mathrm{kg\,m^2}$. The flywheel is 0.57 kg and 8.07×10^{-4} $\mathrm{kg\,m^2}$.

minimization of the system's moment of inertia and mass with maximization of the flywheel's moment of inertia.

The overall structure and frame of the system consists of a cube with a 20 cm edge and with 4 spikes per face. The spikes include a bend to create a regular octagon with 20 cm on each side. Additional mass was added to balance the vehicle around the rotation axis as well as across the vehicle left to right. No attempt was made to balance the weight around the vertical z-axis on this initial prototype. The design and the geometry of the spikes require a special discussion. Computational studies showed that distributing the contact forces over the maximum area (i.e. direct contact between the vehicle's enclosure and terrain; no spikes) make for the
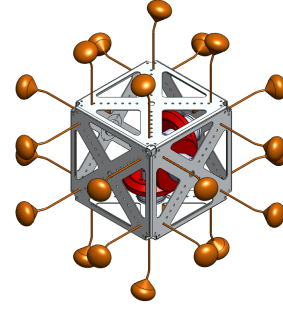

Fig. 8. Second prototype of the hybrid. Note the lilypad design of the tips of the spikes.

most robust mobility in varying terrain conditions (e.g. soft regolith, hard rocks), see [16]. On the other hand, spikes are needed to form a stand-off distance so that solar panels and instruments are protected from unintended impacts with hard rock fragments, and to negotiate large obstacles. As a compromise, spikes should be employed with properly designed feet to increase contact area and avoid sinkage in loose terrain. This design compromise is represented in the second prototype of the hybrid that uses spikes with lilypad-like tips (see Figure 8). Next section discusses experimental results from a 3 degree of freedom (DOF) test stand.

VI. EXPERIMENTAL RESULTS

We performed experiments on a low-gravity 3DOF test stand to further characterize the dynamics of the hybrids and to assess the validity of the models presented in Section III. The test stand consists of a gravity off-load system with pulleys and a counterweight. Two off-load cables are used to prevent rotation about the vertical axis due to gyroscopic precession. The effective gravity is determined both statically, with a high precision scale, as well as dynamically by collecting data while dropping the test vehicle on the stand and measuring its vertical acceleration. Two configurations were used, a 2m test stand and a 5m test stand. Experiments were run by programming a pre-defined acceleration (therefore torque) profile into the Arduino microcontroller (that runs the flywheel's DC motor). The experimental torque profiles were then used in the 3D simulation environment to control a model of the prototype. The goal of these tests was to compare the torque levels at which hopping/tumbling are initiated both during the experiments and in simulation (some disagreement is expected due to modeling approximations and the pendulum dynamics introduced by the pulley mechanism of the test stand). Specifically, if behaviors did not match (e.g. experiment demonstrated tumbling but the simulation did not), then the torque profile would be amplified or attenuated until similar behavior was observed. Figure 9 summarizes the results from the experiment-simulation comparisons. The key result is that an average torque amplification of only 6% is required for the simulation to emulate the experiments.

We also developed a 3 DOF test stand that relies on a

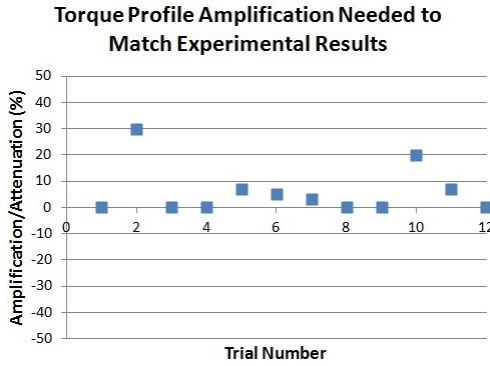**Torque Profile Amplification Needed to Match Experimental Results**

Fig. 9. Experiment-Simulation comparison: values indicate the amount by which the torque profile had to be modified in simulation to match motion observed in experiments. The effective gravity for this set of experiments was 0.235 m/s^2 .
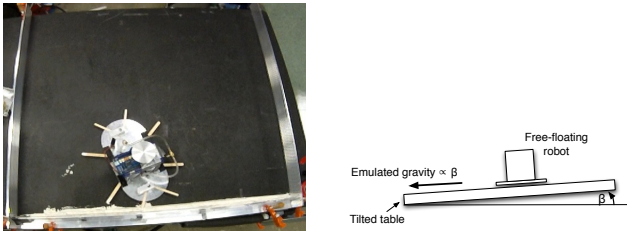

Fig. 10. 3 DOF test stand on a frictionless table; by tilting the granite table, one can create a "small" force that emulates a low gravity field.

frictionless table and does not require any pulley system (and, hence, does not introduce any exogenous dynamics). The test stand consists of a metallic plate that is air-bearing supported over a table and a flywheel attached at the top. The table is slightly tilted in order to emulate a low-gravity environment in 2D (with an emulated gravity of about 0.05 m/s^2), see Figure 10. Baking flour is used as a simulant for regolith found in microgravity environments. We recorded tumbling speeds of ≈ 2 cm/s and hops up to distances of ≈ 0.5 m (longer hops were theoretically possible, but could not be implemented due to the size of the granite table). In general, experimental results on this test stand are in agreement with the results from the pulley system test stand, the analytical model results, and the numerical simulation results; such results, however, are not discussed here due to space limitations.

VII. CONCLUSIONS

In this paper we presented a planetary mobility platform that relies on internal actuation and can perform both long excursions (by hopping) and short, precise traverses (through controlled "tumbles") in low-gravity environments. We have discussed dynamical properties of the platform, planning and control algorithms, the design of a first prototype, and initial experimental results. Collectively, our results lay the foundations for the design of internally-actuated rovers with controlled mobility (as opposed to random hopping motion). This paper leaves numerous important extensions open for further research. First, we seek to refine our planning and

control algorithms to reliably maneuver on rocky terrains and to minimize a given cost criterion (e.g., time or energy expenditure). Second, it is important to develop appropriate contact models for the interaction with loose, granular media typically encountered on small bodies. Third, while we already have first-order estimates (not discussed here due to space limitations) for critical subsystems (e.g., power, thermal, and communication), we plan to refine subsystem design and select an appropriate scientific payload for potential exploration targets (e.g., Phobos). Finally, we plan to develop an actively controlled, 5 DOF test stand that allows for more thorough investigation of motion planning techniques and continued validation of computational models.

REFERENCES

[1] Decadal Survey Vision and Voyages for Planetary Science in the Decade 2013–2022. Technical report, National Research Council, 2011. Available at http://solarsystem.nasa.gov/2013decadal/.

[2] J. C. Castillo-Rogez, M. Pavone, I.A.D. Nesnas, and J.A. Hoffman. Expected science return of spatially-extended in-situ exploration at small Solar System bodies. In *Aerospace Conference, 2012 IEEE*, pages 1 –15, March 2012.

[3] M. Wargo. Strategic knowledge gaps. 2012. Available at http://science.nasa.gov/media/medialibrary/2012/05/04/HEOMD_Strategic_Knowledge_Gaps_--_Mike_Wargo.pdf.

[4] P.M. Cunio, F. Alibay, P. Meira, T. Sheerin, E. Lanford, E. Krupczak, and J.A. Hoffman. Options in the solar system for planetary surface exploration via hopping. In *Aerospace Conference, 2011 IEEE*, pages 1 –10, march 2011.

[5] R.M. Jones. The MUSES–CN rover and asteroid exploration mission. In *22nd International Symposium on Space Technology and Science*, pages 2403–2410, 2000.

[6] M. Chacin, A. Mora, and K. Yoshida. Motion control of multi-limbed robots for asteroid exploration missions. In *Proc. IEEE Conf. on Robotics and Automation*, pages 3037–3042, May 2009.

[7] A. Seeni, B. Schafer, B. Rebele, and N. Tolyarenko. Robot mobility concepts for extraterrestrial surface exploration. In *Aerospace Conference, 2008 IEEE*, pages 1–14, March 2008.

[8] P. Fiorini and J. Burdick. The development of hopping capabilities for small robots. *Autonomous Robots*, 14:239–254, 2003.

[9] C. Dietze, S. Herrmann, F. Kuß, C. Lange, M. Scharringhausen, L. Witte, T. van Zoest, and H Yano. Landing and mobility concept for the small asteroid lander MASCOT on asteroid 1999 JU3. In *61st International Astronautical Congress*, 2010.

[10] R.Z. Sagdeev and A.V Zakharov. Brief history of the Phobos mission. *Nature*, 341:581–585, 1989.

[11] JAXA Hayabusa mission. Technical report, JAXA, 2011. Available at http://hayabusa.jaxa.jp/e/index.html.

[12] D. Scheeres. Close proximity operations for implementing mitigation strategies. In *Planetary Defense Conference: Protecting Earth from Asteroids*, Orange County, CA, February 2004.

[13] T. McGeer. Passive dynamic walking. *The International Journal of Robotics Research*, 9(2):62–82, 1990.

[14] K. Byl and R. Tedrake. Metastable walking machines. *The International Journal of Robotics Research*, 28(8):1040–1064, 2009.

[15] G.W. Howell. *Analysis and control of super-articulated biped robots*. Dissertation, Boston University, 2000.

[16] F. Herrmann, S. Kuß, and B. Schäfer. Mobility challenges and possible solutions for low-gravity planetary body exploration. In *ESA/ESTEC*, Noordwijk, Netherlands, April 2011.

[17] Bellerose. J. and D. Scheeres. Dynamics and Control for Surface Exploration of Small Bodies. In *AIAA/AAS Astrodynamics Specialist Conference and Exhibit*, number 6251, Honolulu, HI, August 2008.

[18] T. Kane, P. Likins, and D. Levinson. *Spacecraft Dynamics*, pages 218–223. The Internet-First University Press, 2005.